Sensitivity of Hail Precipitation to Ensembles of Uncertainties of Representative Initial Environmental Conditions From ECMWF

Xiaofei Li[1,2] (iD), Fuqing Zhang[2] (iD), Qinghong Zhang[1] (iD), and Matthew R. Kumjian[2] (iD)

[1]Department of Atmospheric and Oceanic Sciences, School of Physics, Peking University, Beijing, China, [2]Department of Meteorology and Atmospheric Science, The Pennsylvania State University, University Park, PA, USA

Abstract The sensitivity of hail precipitation from an idealized hailstorm to realistic environmental uncertainties was investigated through ensembles of cloud-resolving simulations using the Weather Research and Forecasting model, with initial condition perturbations derived from the European Centre for Medium-Range Weather Forecasting (ECMWF) operational ensemble. The analyses revealed that hail precipitation rate was very sensitive to small initial environmental perturbations, particularly in thermodynamic variables. The hail precipitation rate was significantly positively correlated with perturbations to the initial potential temperature below 750 hPa and to water vapor mixing ratio above 750 hPa. These small initial perturbations led to subsequent substantial differences in hail precipitation as well as in characteristics of the parent storm (e.g., updraft velocity, diabatic heating, and microphysical processes), all of which play a key role in hail growth. The larger sensitivity of hail precipitation to thermodynamic rather than kinematic environmental initial condition perturbations persisted even when the magnitude of the perturbations was reduced to 10% of the realistic uncertainties derived from the ECMWF ensemble. In the ensemble with reduced-amplitude initial perturbations, there was still a moderately strong positive correlation between hail precipitation rate and the initial perturbations of the thermodynamic variables. However, these sensitivities were nonlinear, suggesting that the intrinsic predictability of hail precipitation rate may be limited, even when environmental uncertainties are reduced to 10%, 1.0×10^{-3}, and 1.0×10^{-5} of the currently realistic magnitude of initial condition uncertainty.

1. Introduction

The difficulty of convective storm predictability in numerical weather forecasts is becoming increasingly problematic as the damage caused by hailstorms intensifies across the world (e.g., Allen & Tippett, 2015; Guan et al., 2015; Punge & Kunz, 2016). Considerable efforts have been made to explore the predictability of severe storms (e.g., Flora et al., 2018; Weyn & Durran, 2017). Ensemble forecasting is now an important component of operational forecasting and is increasingly used at convection-permitting or even higher spatial resolutions (Miltenberger et al., 2018). Past studies have demonstrated the ability of storm-scale ensemble analyses to simulate severe storms (Flora et al., 2018; Potvin et al., 2017; Zhang et al., 2016). However, the critical initial perturbations contributing to variance in the simulated hail precipitation as well as the upper limit of practical predictability of hail remains particularly challenging (Snook et al., 2016), especially in ensemble simulations of hailstorms.

In recently published papers, the predictability and various causes of the loss of predictability of other hazards related to severe storms, including tornadoes, heavy rainfall, severe convective winds, and tropical cyclones, have been quantified using ensemble simulations (Durran & Weyn, 2016; Emanuel & Zhang, 2017; Fernández-González et al., 2017; Flora et al., 2018; Miglietta et al., 2016, 2017; Munsell et al., 2017; Nielsen & Schumacher, 2016; Weyn & Durran, 2017, 2018; Zhang et al., 2015, 2016; Zhang & Tao, 2013). For example, the practical and intrinsic predictability of a tornadic supercell have been explored from the perspective of convection initiation time, which was strongly modulated by the evolution of the planetary boundary layer, and local topography (Zhang et al., 2015, 2016). Miglietta et al. (2016, 2017) found that due to orography, large-scale forcing and model initialization time had a substantial impact on rainfall in a supercell and that its predictability can be extended when topographic features are responsible for convection initiation. The impact of initial condition uncertainty on the ensuing forecasts of supercells was evaluated using a perfect

model assumption (Flora et al., 2018). Predictability was substantially limited by forecast storm location uncertainty and ensemble bifurcations in forecast storm intensity.

However, direct prediction of hail has received relatively little attention due to the challenges involved in numerical weather prediction, model treatments of convective storms, and microphysical parameterizations (Dennis & Kumjian, 2017; Morrison et al., 2009; Snook et al., 2016). For example, the evolution of a hail-producing convective storm can occur over time scales as small as minutes, necessitating small time steps. Hail in numerical models is treated in bulk using parameterization schemes (e.g., Morrison & Milbrandt, 2011), which are incapable of explicitly simulating hail sizes and instead only predict bulk moments of the hail size distribution. Further, some microphysical processes important for hail (e.g., wet growth, sedimentation, and melting) are not adequately treated by such schemes. In addition, the different kinds of physical schemes need to be well matched with the predicted motion and intensity of the convective storms (Snook et al., 2016). The predictability of hail is also limited by the estimation of the uncertainty in atmospheric state, which truly is the initial condition uncertainty. This has been less extensively studied with the necessary ensemble perturbations. Small initial condition errors can lead to vastly different intensity forecasts due to the presence of moist convection (Zhang & Sippel, 2009; Zhang & Tao, 2013), which suggests that, at least for some storms, the intensity forecasts may be of intrinsically limited predictability.

Weyn and Durran (2017) discussed uncertainties, recast as the "butterfly effect" (Lorenz, 1969), and proposed that certain deterministic systems in the atmosphere have a finite range of predictability that cannot be extended by reducing the magnitude of initial condition errors to any value greater than zero. However, the system needs to be small in scale for the initial condition errors to constrain the intrinsic predictability of the atmosphere (Weyn & Durran, 2017). Reducing the amplitude of the initial condition errors can improve predictability lead times, but this improvement diminishes with further reductions in the error amplitude. This suggests a limit to the intrinsic predictability of mesoscale convective systems, which are often thought to be particularly effective at transferring small-scale perturbations to larger scales (Weyn & Durran, 2017; Zhang et al., 2006). In Zhang et al. (2016), a tornadic supercell's intrinsic predictability limit was found to be 3–6 hr using an ensemble generated from small-magnitude perturbations. Substantial reductions in the forecast spread of the supercell structure were found in sensitivity simulations by Flora et al. (2018) that reduced the magnitude of spread of their original initial conditions. However, relatively few studies have paid attention to the uncertainties in forecasts of high-impact hazards produced by supercells, including hail, and reduced initial condition errors have not yet been imposed on simulations of a hailstorm to examine the predictability of hail and compare it to the predictability of total precipitation. In past studies, ensembles were generated by shifting the initialization time (Miglietta et al., 2016; Zhang et al., 2015). By contrast, few studies have generated initial conditions from storm-scale ensemble analyses. Cintineo and Stensrud (2013) generated an ensemble with realistic perturbation magnitudes and structures from a 6-month composite of supercell environments onto a basic initial sounding for supercells to investigate practical predictability of the storm features. In contrast to this type of "climatological uncertainty," however, a real-time ensemble perturbation from instantaneous initial condition uncertainty drawn from the prestorm environment, which we call "flow-dependent" uncertainty, has never been applied to an idealized storm to investigate its uncertainty. Flora et al. (2018) is one of the first studies to use storm-scale ensemble analyses as initial conditions to explore storm-scale predictability. Nevertheless, few studies pay attention to the uncertainty of high-impact hazards produced by supercells, including hail. The initial condition perturbations used in this study were derived from operational ensemble prediction systems from the European Centre for Medium-Range Weather Forecasting (ECMWF) model to provide realistic atmospheric perturbations (Molteni et al., 1996). Then, these are separated by type of perturbation (thermodynamic or kinematic) and coupled to idealized hailstorm simulations using the Weather Research and Forecasting (WRF) Model, version 3.7.1 (National Center for Atmospheric Research, 2015), to obtain higher resolution.

We assessed both practical and intrinsic predictability of hail precipitation rate using idealized ensemble hailstorm simulations. The details of the method used to generate perturbations in the ensembles and the experimental design are provided in section 2. In section 3, we present simulations in which the thermodynamic and kinematic initial condition perturbations were applied to isolate the sensitivity of ensemble forecasts of hail precipitation rate to uncertainties in the initial conditions. First, the leading effects of the initial perturbations were examined using the top 10 and bottom 10 members, ranked by hail

precipitation rate. Second, we explored the uncertainty in hail precipitation rate as well as number of grid points that experienced hail precipitation by producing several sets of ensembles using the original and reduced-magnitude initial condition perturbations. Section 4 is a discussion and conclusions of this work.

2. Ensemble Simulation Design

The advanced version of the WRF model version 3.7.1 (National Center for Atmospheric Research, 2015) was used for all simulations. We used the same model setup and physical configurations as in X. Li et al. (2017). The initial cloud condensation nuclei concentration was fixed at 700 mg^{-1} below 2 km above ground level and decreased exponentially to the model top; this cloud condensation nuclei profile is a typical continental distribution for this area (Duan et al., 2012; X. Li et al., 2017). All simulations were configured with 500-m horizontal grid spacing and 51 vertical levels. We used the National Severe Storms Laboratory 2-moment microphysics scheme (Mansell et al., 2010; Mansell & Ziegler, 2013) because of its more sophisticated treatment of hail growth processes than other schemes and the ability to provide realistic storm structures for this case (X. Li et al., 2017).

The prestorm environment was favorable for deep moist convection (X. Li et al., 2017), with sufficiently large values of convective available potential energy (CAPE) analyzed in the ECMWF ensemble mean ahead of a convergence line (Figure 1a), with strong southerly flow advecting in warm (Figure 1c), moist air. All simulations were initialized with the same reference idealized input sounding from 0600 UTC on 30 June 2013 (X. Li et al., 2017) at the location of the marker in Figure 1. This was treated as the control member state. In part, this sounding was chosen for the base state because there was no observed representative sounding available for this case and because it has much higher vertical resolution than has the ECMWF ensemble (which only has eight vertical levels available). However, the ECMWF ensemble allows for assessment of the environmental variability around the location of the hailstorm: The standard deviation of CAPE for the 50 ensemble members was >250 J/kg (Figure 1b), and the standard deviation of the surface air temperature was about 1.0 K (Figure 1d).

A key benefit of using ensembles is that they provide more complete information regarding the possible uncertainty in the atmospheric state than can be constructed using a single forecast. Ensemble perturbations from the 0-hr forecast ECMWF operational 50-member ensemble were used to simulate the impact of realistic uncertainties in real-time initial conditions on hail precipitation from an idealized storm simulation. Ensembles from the ECMWF include perturbations of the initial conditions that are based on the assertion that the main source of model errors (i.e., the unstable growth of representative initial errors) occurs at midlatitudes (Molteni et al., 1996). These ensemble members have horizontal grid spacing of 0.5° × 0.5°, with eight vertical levels on isobaric surfaces.

To generate instantaneous initial ensemble input soundings, we took the difference in vertical profiles of potential temperature, water vapor mixing ratio, and U- and V-wind components between each of the 50-member ECMWF ensemble and the ensemble mean for the model grid point closest to the observed hailstorm location and at the time of 0000 UTC on 30 June 2013, just prior to its formation (Figure 1; see X. Li et al., 2017, for details of the observed storm). Then, these 50 profiles of differences were interpolated to the control input sounding height levels and added to the control input sounding to obtain 50 initial perturbed soundings, named EC_All. The across-ensemble variability of the CAPE for the initial ensemble soundings (about 290 J/kg) had a similar magnitude to the environmental variability and much less than one fourth of the ensemble mean (which was >1,200 J/kg; see Table 1).

Use of this type of perturbation, which we call flow-dependent uncertainty, differs from the climatological uncertainty used by Cintineo and Stensrud (2013). In that paper, perturbations were obtained from supercell environments taken over a 6-month period preceding the event. In contrast, here we focus on the sensitivity of hail precipitation to the real-time uncertainty of the atmospheric state for a given event. The magnitudes of the perturbations were much smaller than the mean of the 50 members (Figure 2) and are comparable to 1-hr forecast error in Cintineo and Stensrud (2013). For example, the maximum standard deviation of water vapor mixing ratio perturbations was <1.0 g/kg, or only about 10% of the maximum mean value (cf. Figures 2a and 2c), and the maximum standard deviation of total wind speed perturbations was <1.5 m/s, which is much less than the mean wind speed (cf. Figures 2b and 2d). These standard deviations provided
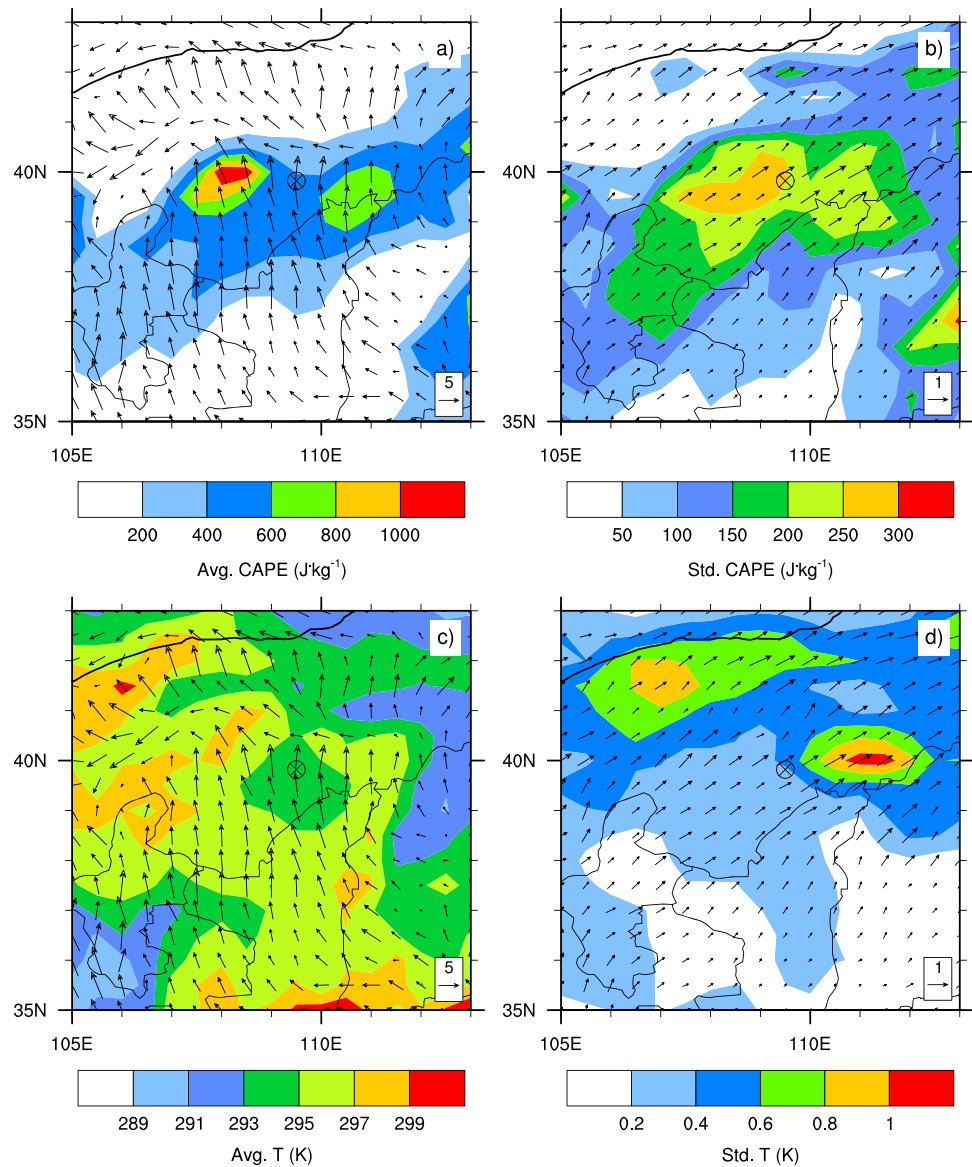
Figure 1. (a) Ensemble mean convective available potential energy (CAPE; in J/kg), (b) standard deviation of CAPE (in J/kg), (c) ensemble mean of surface air temperature (in K), and (d) standard deviation of surface air temperature (in K) for the 50 European Centre for Medium-Range Weather Forecasting ensemble analyzed members from 0000 UTC on 30 June 2013. The marker shows the location of the control sounding (X. Li et al., 2017). Vectors represent the (a and c) ensemble mean and (b and d) ensemble spread (Std. U + Std. V) of 10 m above ground level wind.

realistic and vertically systematic perturbations, at least as determined from the ECMWF. Note that we choose to perform the analysis using the wind speed magnitude and vertical wind shear rather than U- and V-components of the wind individually because the former are both Galilean invariant. The total wind speed was calculated by the absolute value of the vector wind and wind shear was calculated by the absolute value of vector wind at any altitude minus the surface wind. We conducted additional simulations isolating the thermodynamic (potential temperature and water vapor mixing ratio) and kinematic (total wind speed and vertical wind shear) perturbations individually to assess the main factors contributing to the uncertainties in hail precipitation, named EC_TQ and EC_UV, respectively.

Table 1
Ensemble Mean and Ensemble Spread of the Convective Available Potential Energy (CAPE) From the Sets of EC_All and EC_10%All

	CAPE (J/kg)	
Ensemble	Average	Standard deviation
EC_All	1,276	291
EC_10%All	1,260	30
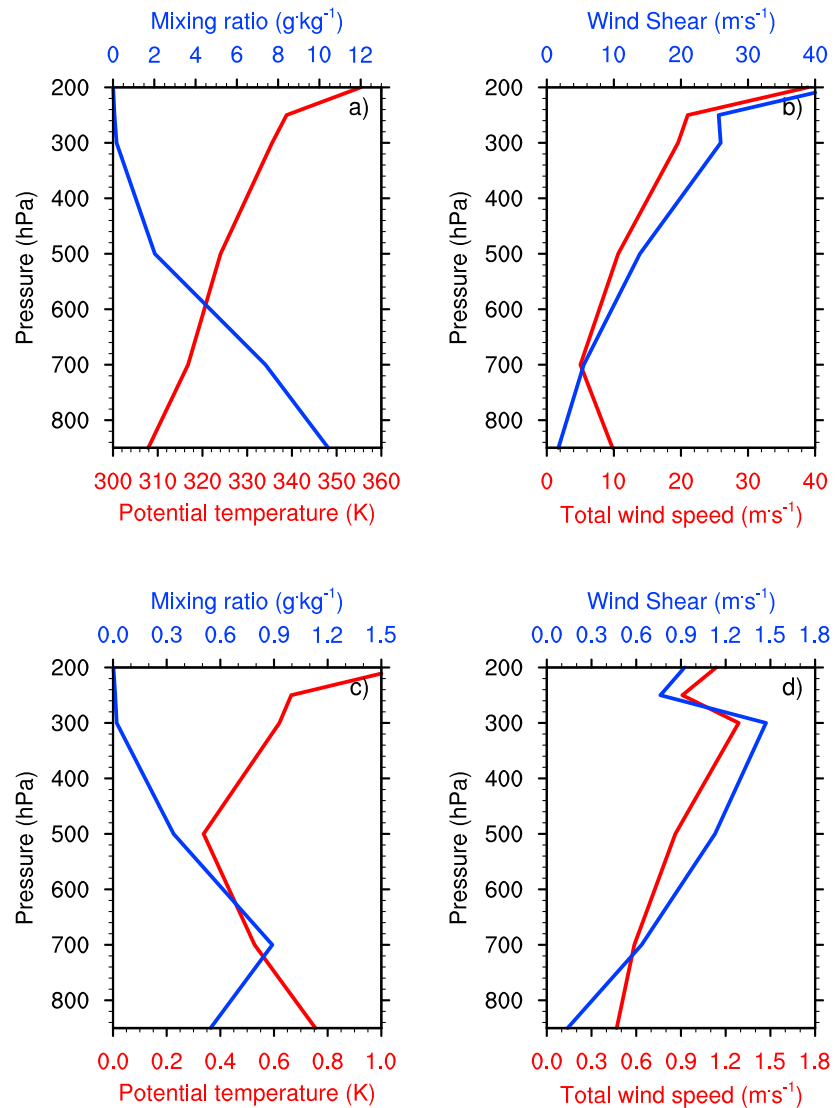
Figure 2. Vertical profiles of (a, b) means and (c, d) standard deviations for (a, c) thermodynamics variables (mixing ratio of water vapor [blue] and potential temperature [red]) and (b, d) kinematic variables (wind shear [blue] and total wind speed [red]) from the 50 European Centre for Medium-Range Weather Forecasting members. Wind shear was calculated as the difference between the vector wind at any altitude and the vector wind at the ground.

These original initial condition perturbations are representative of practical predictability. However, the intrinsic predictability of hail precipitation remained unclear, so it was necessary to investigate if reducing the magnitude of these initial condition perturbations would linearly reduce the uncertainty of the hail precipitation rate. Previously, Flora et al. (2018) found a nonlinear response when reducing initial condition uncertainty in an ensemble of supercell simulations. The same three sets of simulations described above were repeated, but with the initial ensemble perturbations reduced to 10% of their original magnitudes to investigate the intrinsic predictability limit of hail precipitation. These 50-member ensemble simulations are named EC_10%All, EC_10%TQ, and EC_10%UV, respectively. Further, to investigate the uncertainty of hail precipitation and its intrinsic predictability limit under even much small initial condition perturbations, we ran two additional simulations with the original perturbation magnitude reduced to 1.0×10^{-3} and 1.0×10^{-5} of the original perturbation, named EC_10^{-3}All and EC_10^{-5}All, respectively.
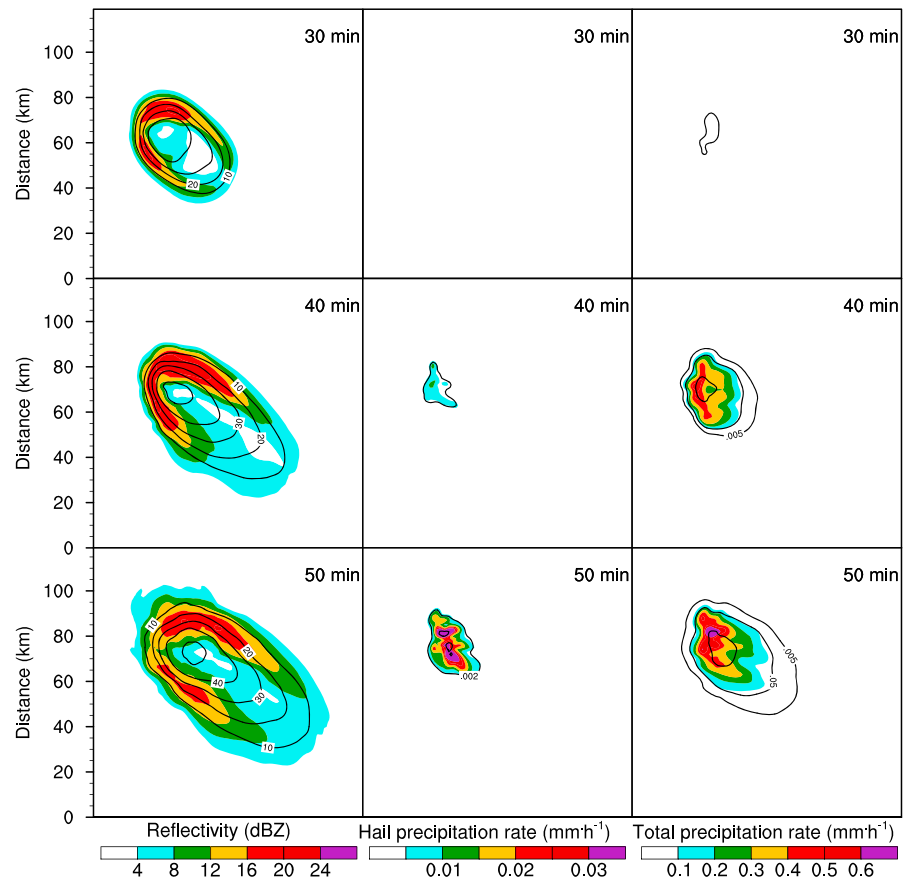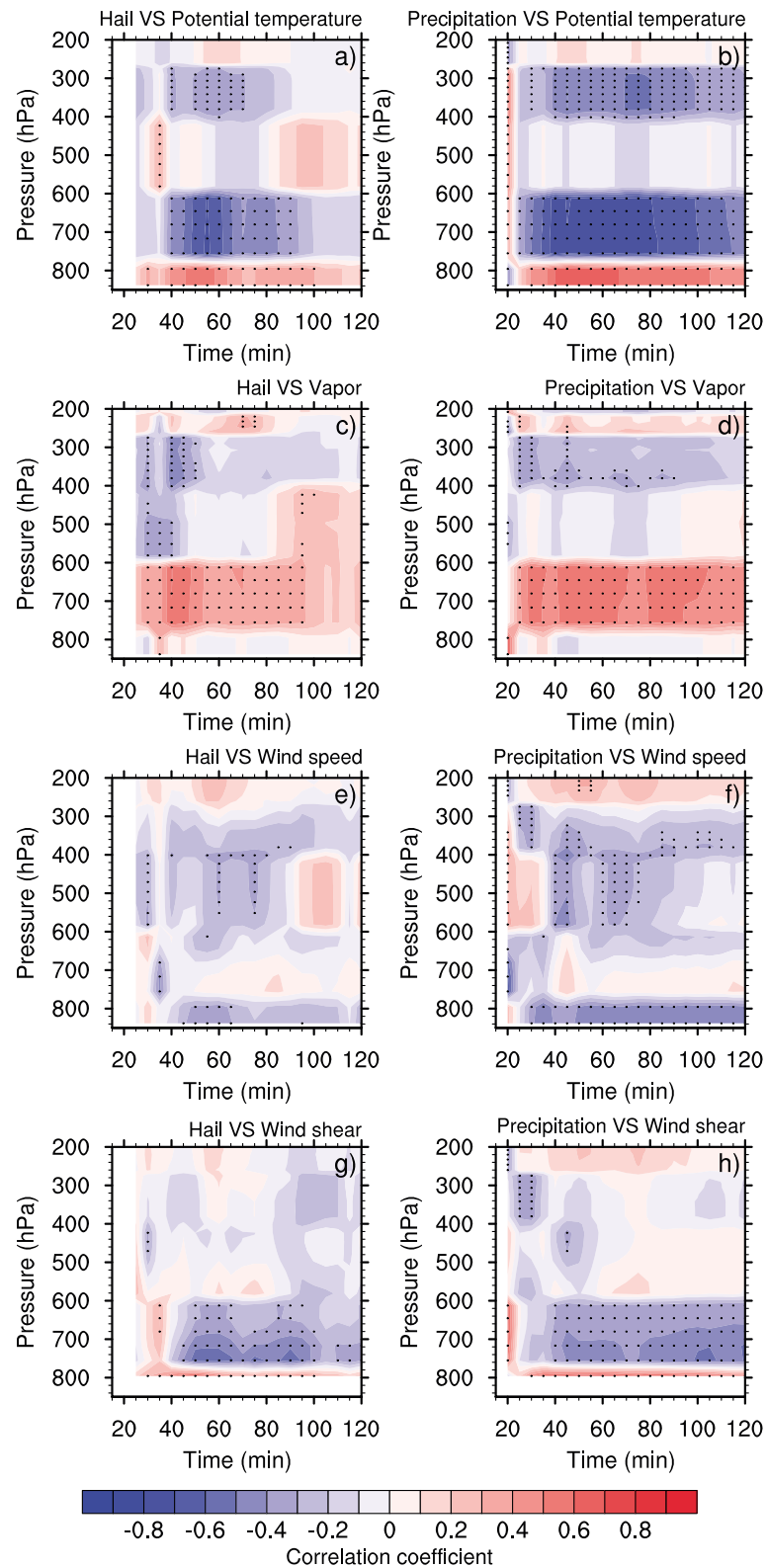
Figure 3. Black contours show the ensemble mean of (left column) simulated composite radar reflectivity factor (in dBZ), (middle column) hail precipitation rate (in mm/hr), and (right column) total precipitation rate (in mm/hr); shading shows the standard deviations of each quantity; output is shown for the EC_All ensemble at (top row) 30 min, (middle row) 40 min, and (bottom row) 50 min.

3. Results

To examine the sensitivity of realistic initial condition perturbations to simulated hail precipitation rate, we began with the EC_All ensemble. The evolution of ensemble means and their standard deviations of simulated composite radar reflectivity factor, hail precipitation rate, and total precipitation rate for EC_All are presented in Figure 3. The ensemble mean had the classic behavior of a supercell during its mature stage, featuring a southeastward movement (right of the mean wind). The ensemble mean total precipitation in excess of 0.005 mm/hr first appears at 30 min and increased substantially from 40 to 50 min, whereas the ensemble mean hail precipitation rate in excess of 0.002 mm/hr appears later, with its extension and intensity being much smaller than that of total precipitation. The maximum standard deviation of simulated composite radar reflectivity was about 16 dBZ, confined mainly to the edges of the ensemble mean centroid (indicating some spread in storm location). The standard deviations of hail and total precipitation rates reached their peak values of about 1.0 and 12 mm/hr, respectively, near the hailstorm center, which implies a considerable ensemble spread for hail and a relatively small ensemble spread for total precipitation compared to their ensemble means.

To investigate the sensitivity of hail precipitation rate to initial thermodynamic and kinematic perturbations, correlations between both the surface hail and total precipitation rates and the initial sounding throughout the vertical levels were calculated (Figure 4). The increase in the hail precipitation rate was strongly correlated with thermodynamic factors, including an increase in potential temperature at the surface with a decrease above 750 hPa (Figure 4a). A strong positive correlation was found for hail rate and the water vapor mixing ratio between 750 and 600 hPa during the mature stage (40–60 min) of the hailstorm (Figure 4c).

AGU
100
ADVANCING EARTH
AND SPACE SCIENCE

Journal of Geophysical Research: Atmospheres

10.1029/2018JD029899

**Figure 4.** Time-height plots showing the correlations between each initial sounding factor (a and b, potential temperature; c and d, water vapor mixing ratio; e and f, total wind speed; and g and h, wind shear) and the (left) domain mean hail precipitation rate and (right) total precipitation rate among the 50 members of the EC_All ensemble. The black dots represent a significance level above 95%.
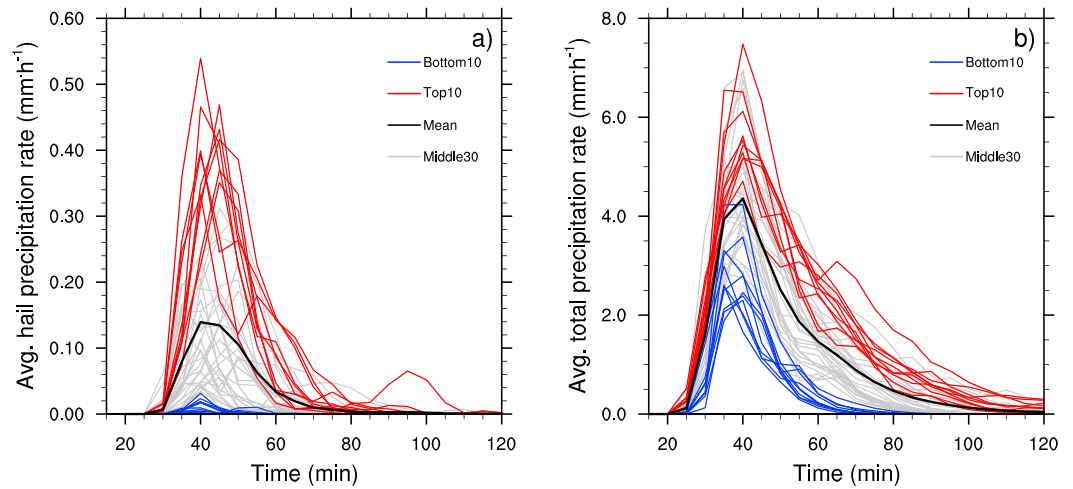
Figure 5. Time series of mean surface (a) hail precipitation rate and (b) total precipitation rate for each member of the 50 EC_All runs. The members with the top 10 largest hail precipitation rate (Top10) are marked by the red lines, whereas the bottom 10 members (Bottom10) are marked by the blue lines. The Middle30 members are marked by the gray lines. The average was calculated for a region where hail precipitation rate was greater than 0 mm/hr. The group members in the Top10 and Bottom10 groups for total precipitation rate are the same as those for hail precipitation rate.

However, the kinematic perturbations exhibited different and relatively weak correlations, including some negative correlations with total wind speed below 750 hPa and above 600 hPa after 40 min, as well as positive correlations with low-level wind shear that became negative from 750 to 600 hPa (Figures 4e and 4g). There was a similar pattern in the significant correlations with the surface total precipitation rate, as shown in the
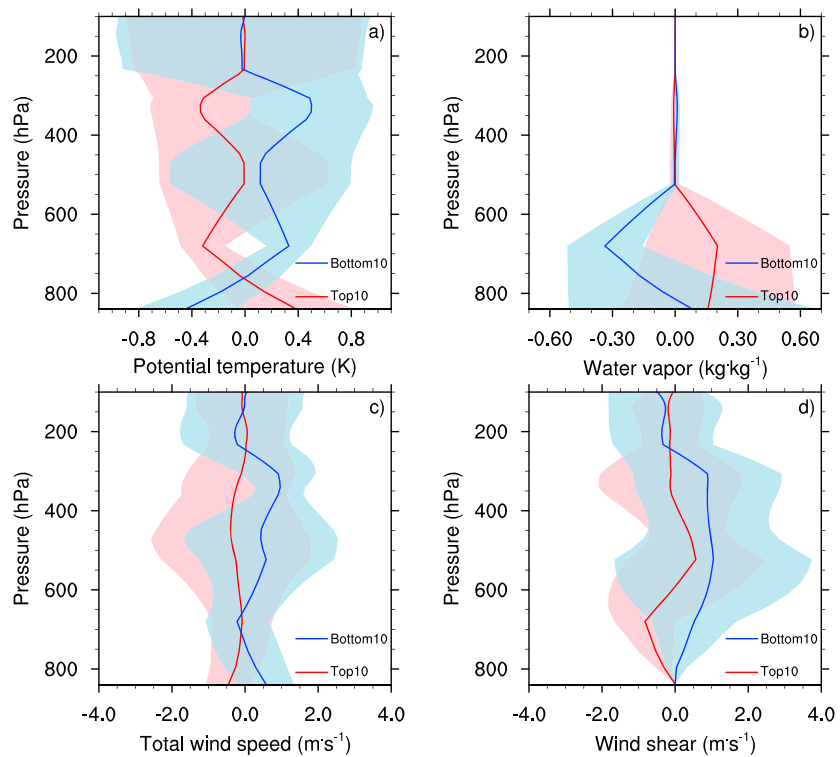
Figure 6. Vertical profiles of the differences for the top 10 members (red line) and the bottom 10 members (blue lines) for each of the four initial sounding factors. The differences represent the mean of top 10 or bottom 10 minus the mean of 50 members in EC_All for the initial time. The shaded regions indicate ±1 standard deviation.
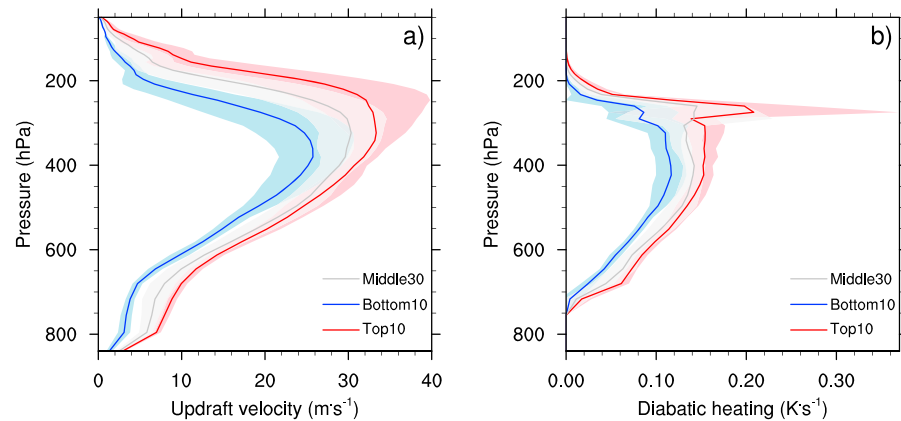
Figure 7. Vertical profiles of domain maximum (a) updraft velocity and (b) diabatic heating from microphysical processes (condensation, deposition, and freezing) over the Top10 members (red lines), Bottom10 members (blue lines), and Middle30 members (grey lines) from 30 to 60 min. Shaded region is ±1 standard deviation, adding to the mean values.

right panels of the figure. Increases in precipitation are even more strongly correlated with increasing of moistening between 750 and 600 hPa than are the increases in hail (Figures 4c and 4d), which we speculate is because increases in moisture likely reduce the entrainment of dry air, strengthening the overall storm. The correlation of the total precipitation rate with thermodynamic factors is stronger and longer lasting than the correlation with kinematic factors. This suggests that, unsurprisingly, the increase in potential temperature at the surface and the decrease in higher layers (i.e., destabilization of the troposphere) and accompanying increase in humidity above 750 hPa were favorable for increased storm intensity and thus precipitation production. The resulting larger amount of available supercooled liquid water (e.g., Kumjian et al., 2012) would be favorable for increased hail production.

In each EC_All member simulation, the conditionally averaged hail precipitation (averaged for regions where hail precipitation rate was >0 mm/hr) had a similar evolution, mostly starting after 20 min with increasing and maximum values from 30 to 60 min. This behavior was captured by the ensemble mean, as well (Figure 5, black curve). However, the members displayed considerable spread in peak values of hail precipitation rate. The members in the EC_All set were separated into Top10 (i.e., those with the top 10 largest hail precipitation rates), Bottom10 (those with the 10 smallest hail precipitation rates), and Middle30 groups (those with the 30 middle hail precipitation rates; Figure 5a, red, blue, and gray lines, respectively). We focus

Table 2
Results From Paired-Samples t Tests for the Mean of Variables in Figures 7–9, Including the Correlation of Top10 and Bottom10 and the Differences Between Top10 and Bottom10, Where p < 0.1 Represent a Significant Result Over 90% Significance Testing

|	Top10 and Bottom10		Top10 − Bottom10			
Variable	Correlation coefficient	p for correlation	Mean	Standard error	t	p (two tailed)
Updraft velocity	0.898	0.000	5.635	0.797	8.651	0.000
Microphysical latent heating	0.952	0.000	0.029	0.004	5.454	0.000
Qcloud	0.995	0.000	1.634	0.231	4.693	0.000
Qrain	0.985	0.000	1.324	0.187	4.197	0.000
Qice	0.726	0.000	6.701	0.948	2.992	0.004
Qsnow	0.940	0.000	5.044	0.713	4.035	0.000
Qgraupel	0.960	0.000	7.231	1.023	5.484	0.000
Qhail	0.881	0.000	0.424	0.060	5.148	0.000
Vapor deposition	0.859	0.000	0.203	0.029	3.624	0.001
Cloud collection	0.896	0.000	10.574	1.495	3.686	0.001
Rain collection	0.942	0.000	8.469	1.198	3.182	0.003
Ice collection	0.740	0.000	0.246	0.035	3.448	0.001
Snow collection	0.828	0.000	0.413	0.058	3.879	0.000
Graupel conversion	0.844	0.000	3.768	0.533	1.738	0.088
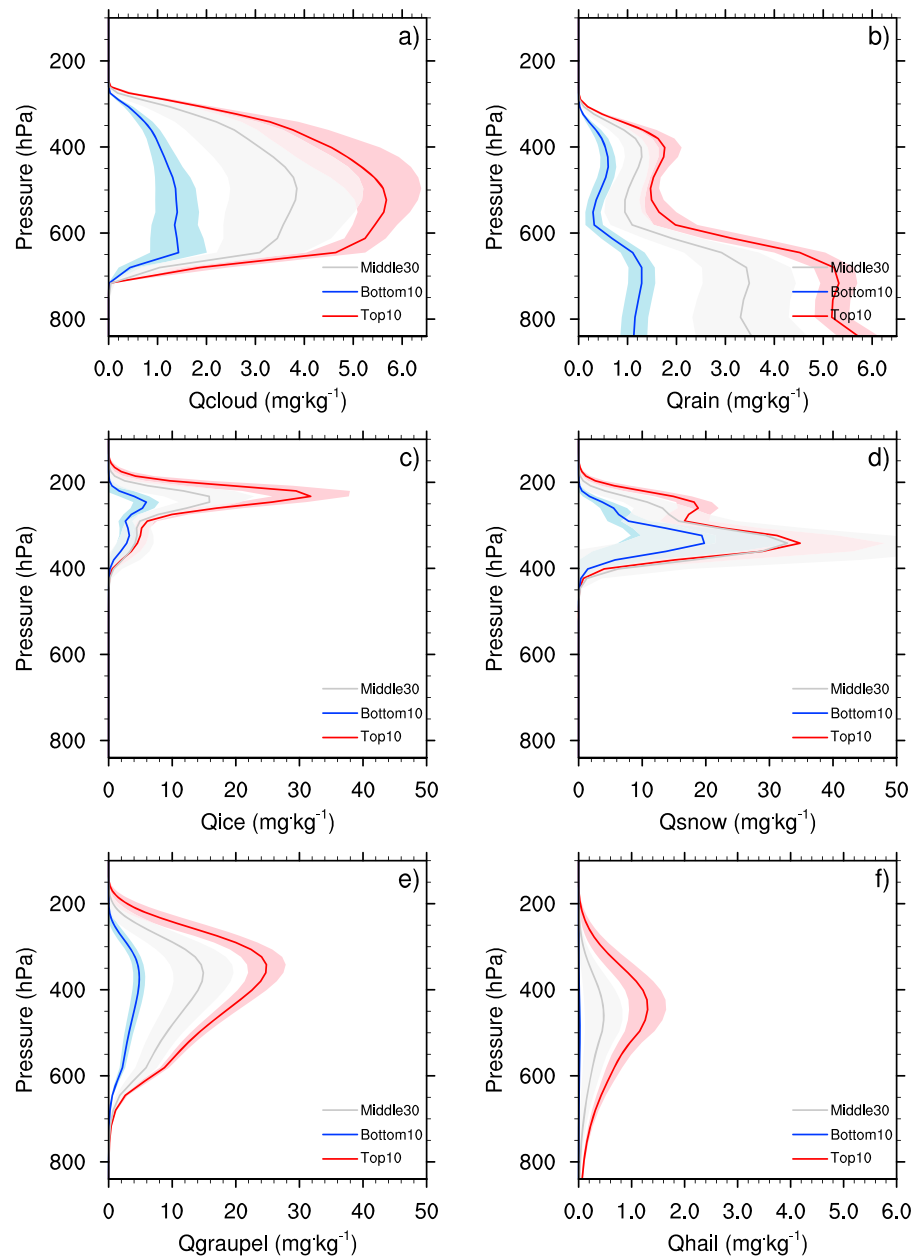
Figure 8. Same as Figure 7, but for the domain-averaged mixing ratios of the six hydrometeors: (a) cloud, (b) rain, (c) ice, (d) snow, (e) graupel, and (f) hail.

on hail precipitation rate because it proved meaningful for comparing numerical simulations (M. Li et al., 2017). Each group represents a quintile of the ensemble; quintiles are used here to exemplify the range of uncertainties and to determine the underlying factors that drive the divergence of the two extreme quintiles (e.g., Munsell & Zhang, 2014). The strongest 10 hail precipitation-producing members are not exactly the same as the strongest 10 total precipitation-producing members (Figure 5b), where many storms in the Middle30 produce total precipitation amounts similar to those of the Top10 and a few of the Bottom10 members create total precipitation amounts close to the ensemble mean. Nevertheless, the Top10 and Bottom10 members tend to somewhat above, and well below, the ensemble mean of total precipitation rate (Figure 5b). The peak average hail rates in the Top10 group were all >0.3 mm/hr, whereas those in the Bottom10 group were all <0.03 mm/hr (Figure 5a), indicating a substantial difference between the two groups.
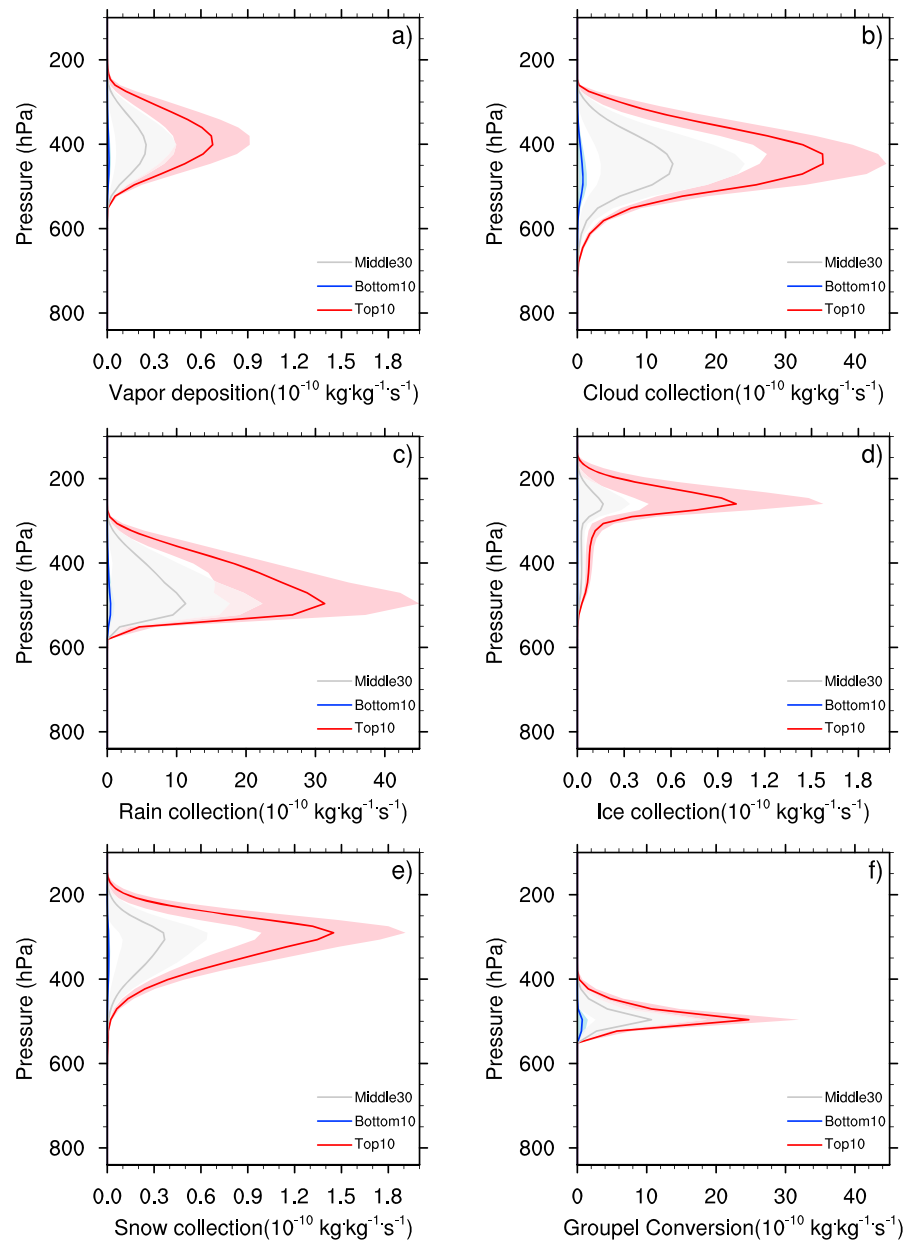
Figure 9. Same as Figure 7, but for six domain-averaged microphysical processes that contribute to increased hail mass, including (a) vapor deposition onto hail, (b) collection of cloud droplets by hail, (c) collection of rainwater by hail, (d) collection of ice crystals by hail, (e) collection of snow by hail, and (f) conversion of graupel to hail.

Figure 6 shows the perturbations for the Top10 and Bottom10 groups. The Top10 members had a more unstable potential temperature profile, with greater moisture content than the Bottom10 members. In addition to hail precipitation rate, substantial differences between the Top10 and Bottom10 member simulations are also found in the parent storms themselves. We compared the simulated updraft velocity and the diabatic heating from microphysical processes (condensation, deposition, and freezing of liquid water) between the Top10 and Bottom10 groups; the differences between the two groups were considerable throughout the vertical profile (Figure 7), indicating that these properties were significantly affected by the small initial condition perturbations. The updraft velocity from the surface to the top of the hailstorm in the Top10 group was significantly different from that in the Bottom10 (Table 2), although the spread of values was similar between the groups. The ensemble mean reached a large peak updraft speed of >30 m/s in the Top10
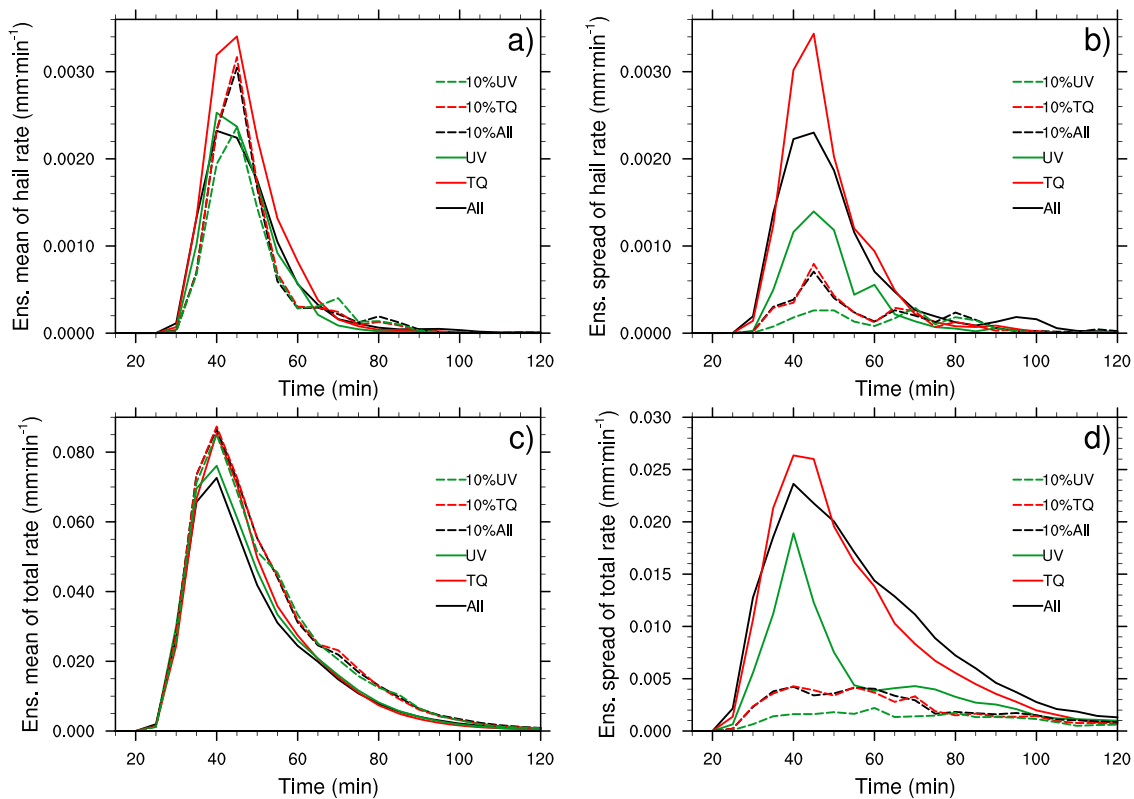
Figure 10. Time series of the (left) ensemble mean and (right) ensemble spread of the domain-averaged (a and b) surface hail precipitation rate and (c and d) total precipitation rate for the 50 runs of EC_All, EC_TQ, EC_UV, EC_10%All, EC_10%TQ, and EC_10%UV.

group at a height of about 300 hPa, whereas it was about 25 m/s at a lower height of about 400 hPa in the Bottom10 group. The maximum updraft accelerations in Figure 7a are maximized well below the level of diabatic heating shown in Figure 7b, which could be largely a result of strong horizontally localized latent heating around 500–600 hPa. There was also a clear distinction in diabatic heating profiles, with almost no overlap between the two groups, with the Top10 group significantly greater than the Bottom10 group throughout all vertical layers of the hailstorm. In the Top10 group, there was a sharp peak in heating above 300 hPa, corresponding to homogeneous freezing of liquid droplets. As discussed in the next paragraph, this is also related to simulated hail production.

To elucidate the microphysical mechanisms by which hail precipitation rate is affected by small perturbations in the initial conditions, the differences in six kinds of hydrometeors and six hail-increasing processes between the Top10 and Bottom10 groups were also examined (Figures 8 and 9). Small perturbations resulted in tremendous differences between the two groups, with the mixing ratios of all six hydrometeors indicating that they were much more abundant in the Top10 group than in the Bottom10 group (Table 2), although there was an overlap for standard deviation of snow mixing ratio above 400 hPa. The perturbations in the Top10 group led to an enhanced warm-cloud process as evidenced by increased cloud droplet mass (Figure 8a), and, to some extent, raindrop mass (Figure 8b), and also to an enhanced cold-cloud process (Figures 8b–8f). The domain-averaged cloud liquid mixing ratio was almost four times that of the Bottom10 group, with a peak difference in concentration around 500 hPa (Figure 8a), whereas for rain the difference was more than fivefold at low levels (Figure 8b), indicating a larger production of ice and subsequent melting. Because the group members that were in the Top10 and Bottom10 groups for hail precipitation rate are not the same as those in the Top10 and Bottom10 groups for total precipitation rate, the difference of magnification between the Top10 and Bottom10 groups for rain is smaller than that for hail (Figures 8b and 8f). The differences for rainwater in Figure 8b between the Top10 and Bottom10 groups are still obvious since the strongest and weakest hail precipitation-producing members are well above or below the ensemble mean. The large increase in cloud droplet and raindrop mass above the 0 °C level
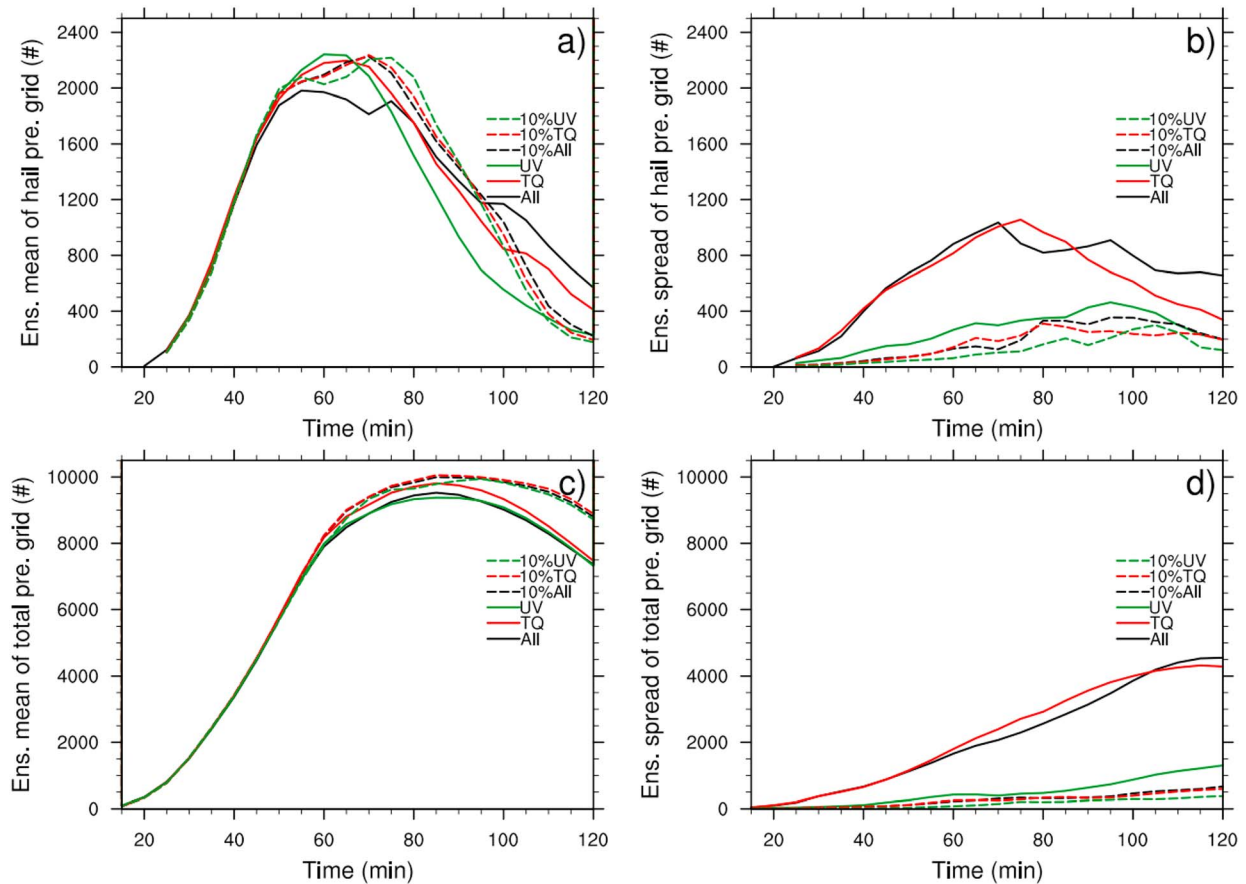
Figure 11. Same as Figure 10, but for (a and b) the number of grid points that experienced hail precipitation and (c and d) the number of grid points that experienced total precipitation.

resulted in a remarkably enhanced riming of hail, including the collection of cloud droplets and rainwater (Figures 9b and 9c), which are the main microphysical processes responsible for hail growth. Additionally, the increased riming rates led to much larger mass of graupel (Figure 8e) and subsequent graupel-to-hail conversion rates (Figure 9f) in the Top10 group. For the ice-phase species, the Top10 group had a larger mixing ratio of ice and snow above 400 hPa (Figures 8c and 8d), which, upon collection of the increased mass of cloud and rainwater, can lead to conversion to graupel. The increase in graupel was important, with the subsequent conversion of graupel to hail around 500 hPa in the Top10 group (Figure 9f), resulting in it being the second most important microphysical process in hail growth. The increased mass of cloud ice and snow aloft in the Top10 group (Figures 8c and 8d) also led to increased hail mass via collection (Figures 9d and 9e), though, along with depositional growth of hail (Figure 9a), these process rates were 1–2 orders of magnitude smaller than the collection of supercooled liquid water and conversion from graupel. This analysis indicates that tiny realistic perturbations in the initial conditions can lead to a radical difference in the production of hail and that the uncertainties in the prediction of hail precipitation remain large.

These initial condition perturbations allowed us to investigate the practical predictability of hail precipitation rate; however, we are also interested in understanding its intrinsic predictability. To do so, we reduced the magnitude of the EC_All perturbations by 10%. As before, we also separated the perturbations by type (thermodynamic and kinematic) to find out what kind of perturbations would result in a larger uncertainty for the idealized hailstorm. To quantify the uncertainty associated with these reduced-magnitude perturbations, we plotted a time series of the ensemble mean and ensemble spread of the domain-averaged hail rate and total precipitation rate along with the original-magnitude perturbations in Figure 10. As with the evolution of the ensemble mean from EC_All, the ensemble mean of the domain-averaged hail and total precipitation rate had a similar temporal evolution in EC_ TQ, EC_UV, EC_10%All, EC_10%TQ, and EC_10%UV
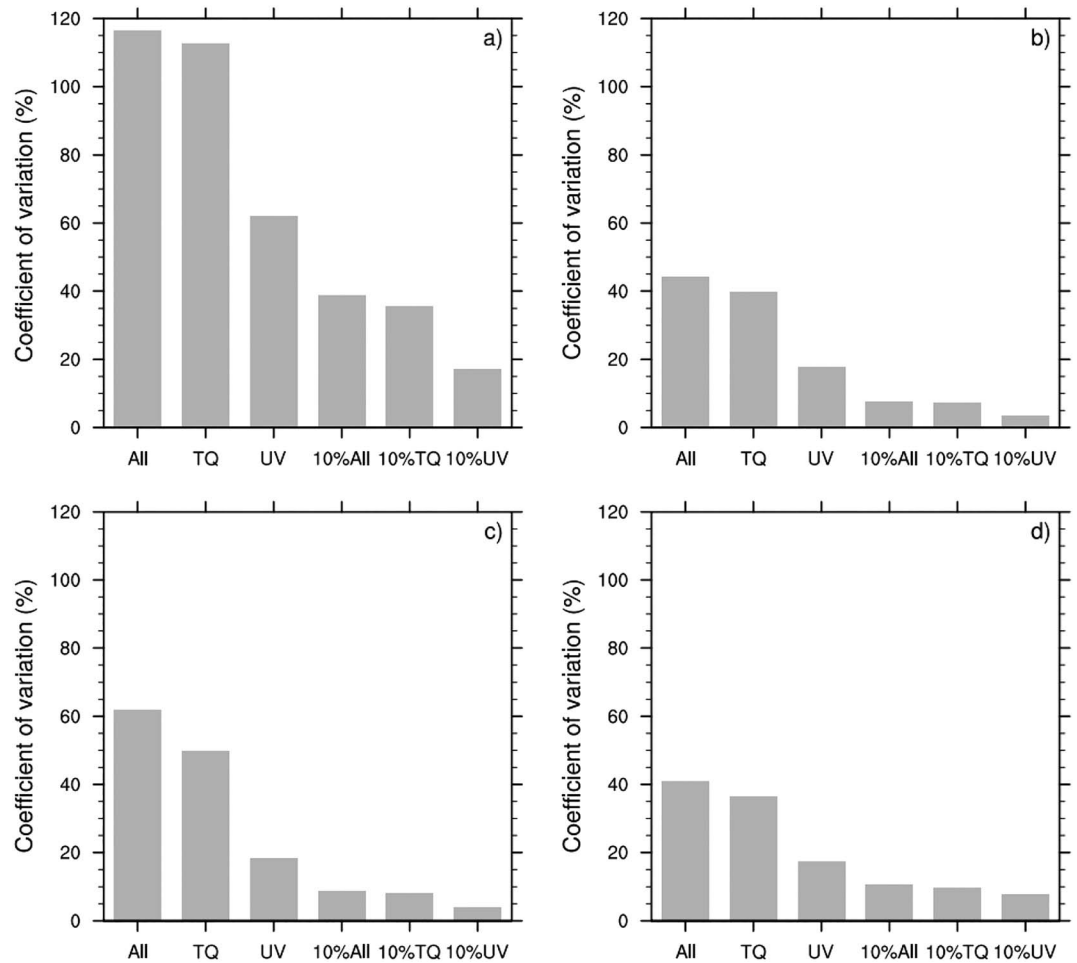
Figure 12. Coefficient of variation for the (a) hail precipitation rate, (b) total precipitation rate, (c) number of grid points that experienced hail precipitation, and (d) number of grid points that experienced total precipitation. The coefficient of variation was calculated by the mean of the ensemble spread divided by the ensemble mean from 30 to 60 min. The number of grid points with accumulated hail precipitation above 0.001 mm and accumulated total precipitation above 0.01 mm were sampled.

(Figures 10a and 10c). However, there were visible differences in the ensemble spread of the six sets (Figures 10b and 10d). For example, the spread of the ensemble when perturbations were reduced to 10% was much less than the spread of the ensemble when perturbations were 100% for both the hail precipitation rate and the total precipitation rate after 30 to 60 min (Figure 10b). EC_TQ had the highest peak value of ensemble spread, and EC_All had the second highest peak value, whereas EC_UV had the lowest peak value among the three original-magnitude perturbation sets, in both ensemble mean and ensemble spread (Figures 10a and 10b). The ensemble spread of EC_All had a comparative peak value to that of EC_TQ for total precipitation rate (Figure 10d). For the three reduced-magnitude perturbation sets, EC_10%All and EC_10%TQ had an almost equal peak value for both the hail rate and the total precipitation rate, whereas they were much larger than the ensemble spread of EC_10%UV. Thermodynamic perturbations generated a larger ensemble spread than did kinematic perturbations, regardless of whether the initial perturbations were of original magnitude or reduced to 10%. There was a similar pattern in the number of grid points that experienced hail precipitation and total precipitation (Figure 11), where the magnitude of the ensemble spread and ensemble mean for the grid points that experienced hail precipitation was smaller than that for the grid points that experienced total precipitation. Additionally, the increase in the peaks of ensemble mean of hail precipitation rate in Figure 10a in the different ensemble groups reveals EC_TQ > EC_10%TQ > EC_10%All > EC_UV >
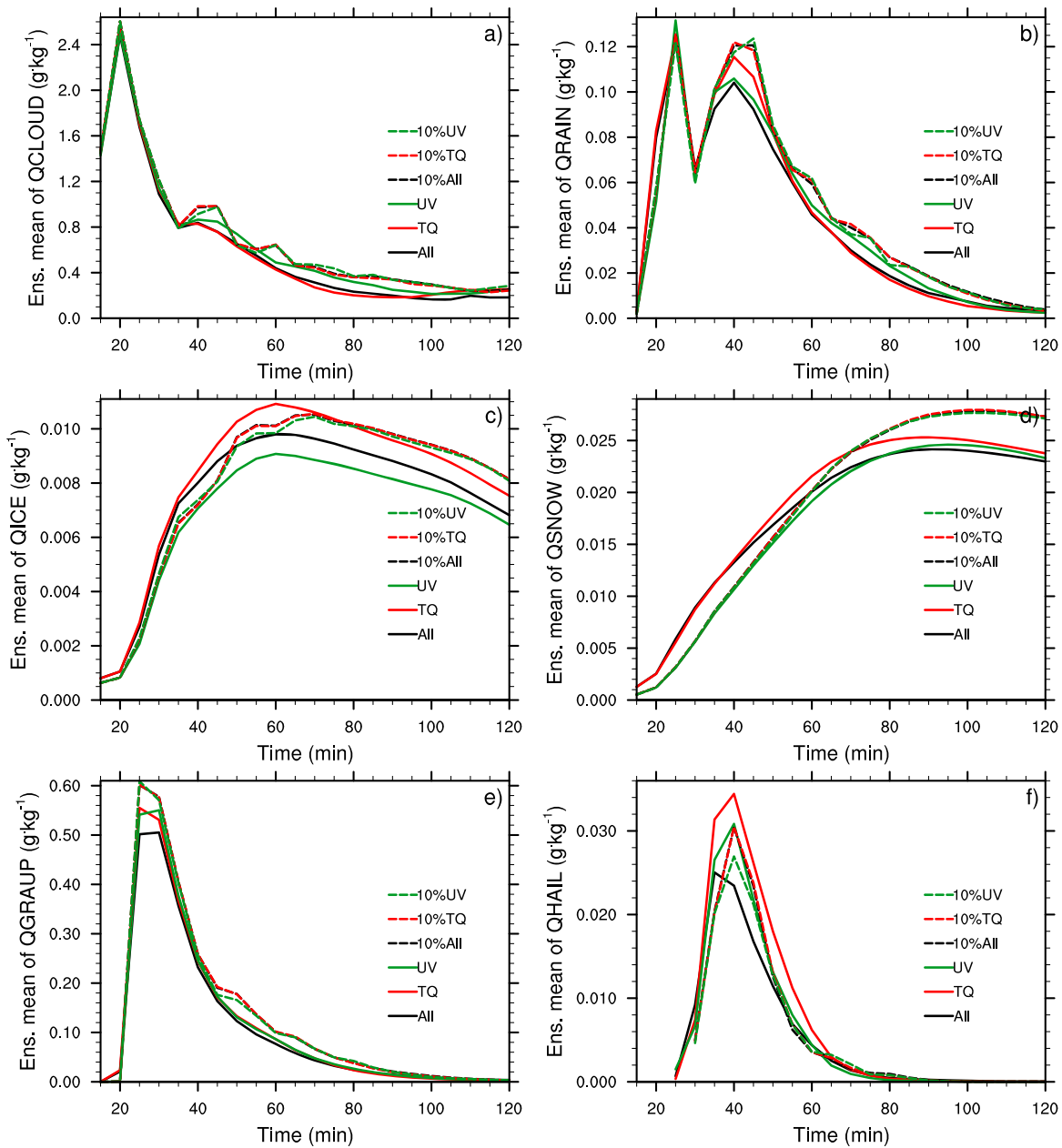
Figure 13. Ensemble mean of the domain-averaged six hydrometeors: (a) cloud, (b) rain, (c) ice, (d) snow, (e) graupel, and (f) hail.

EC_10%UV > EC_All. This suggested that control input sounding for this case represents a rather extreme and near-optimum condition such that any added perturbation may cause a suppressive effect. Therefore, we can infer that the perturbation in this case on average has an overall suppressive effect on hail precipitation compared to EC_All and the dynamic perturbation may suppress more than thermodynamic perturbation for the ensemble mean. The increase in the peaks of ensemble spread of hail precipitation rate in Figure 10b in the different ensemble groups reveals EC_TQ > EC_All > EC_UV > EC_10%TQ > EC_10%All > EC_10%UV. The increasing order in ensemble spread suggested a larger uncertainty in thermodynamic perturbations. With a less than 10-fold reduction in the magnitude of the ensemble spread in EC_10%All, the sensitivity of hail precipitation to initial environmental perturbations was nonlinear, regardless of the rate or number of grid points experiencing hail precipitation, compared to when the initial perturbations were reduced to 10% (Figures 10d and 11d).
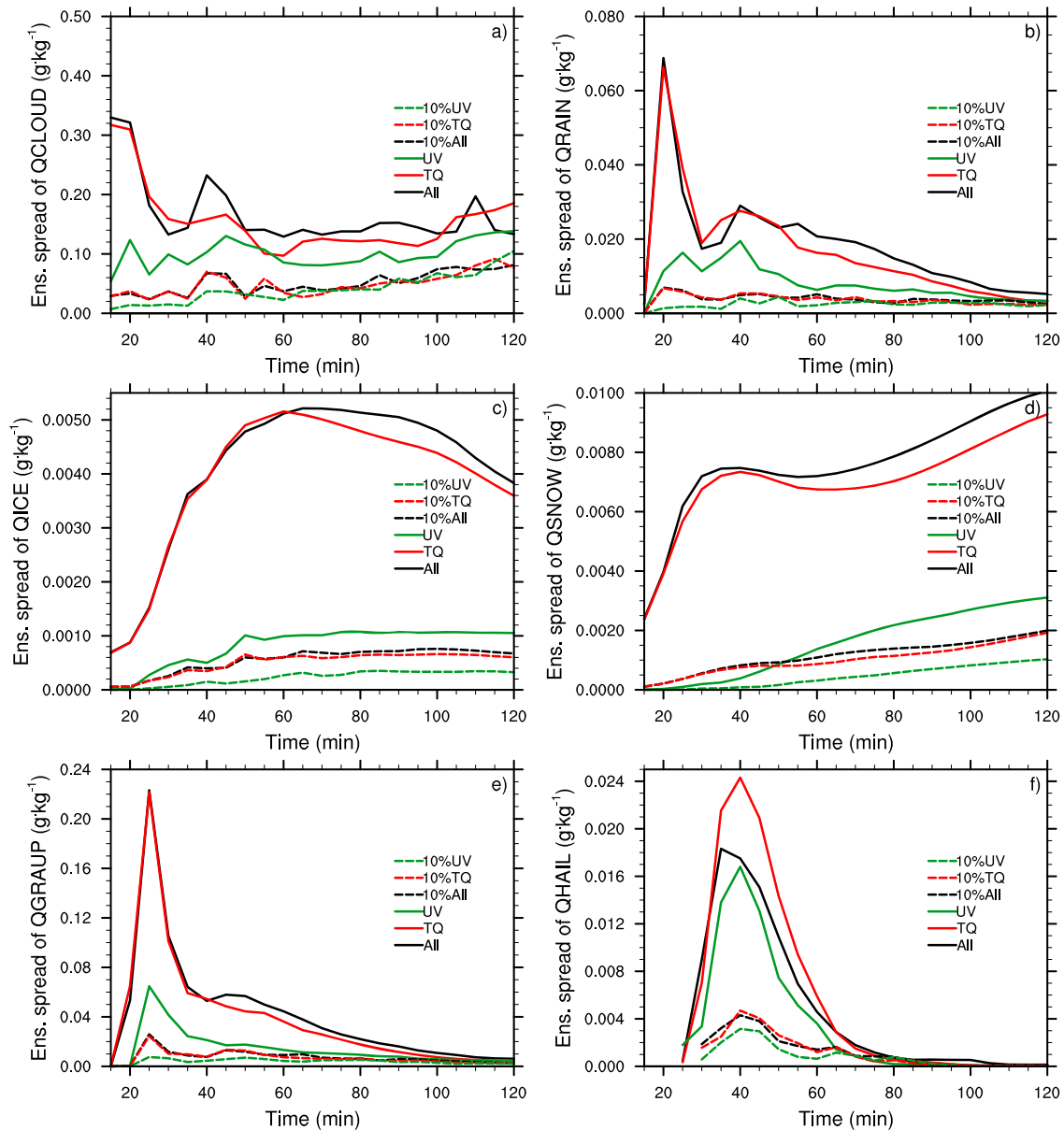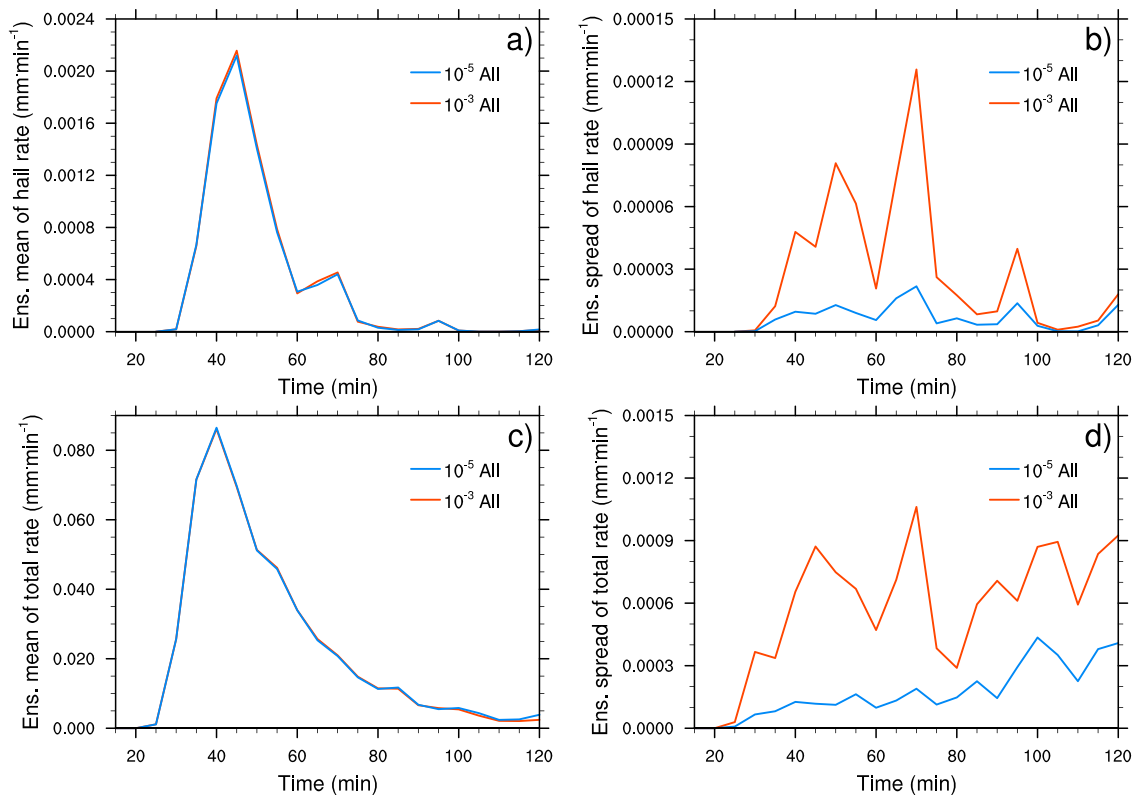
Figure 14. Same as Figure 13, but for the ensemble spread.

To compare the uncertainty of hail precipitation to that of total precipitation, as well as storm area uncertainty, we calculated the coefficient of variation for the precipitation rates and the number of grid points that experienced precipitation from 30 to 60 min (Figure 12). Coefficient of variation in this study was calculated by the average of the ensemble spread over the average of ensemble mean from 30 to 60 min. The coefficient of variation for EC_All and EC_TQ was >100% for the hail rate (Figure 12a), while it was only about 40% for the total precipitation rate (Figure 12b), which suggested that the uncertainty in the hail rate was more than twice that of the total precipitation rate. However, the corresponding figures were about 60% and <20% for EC_UV and EC_10%UV, respectively. A similar difference between thermodynamic and kinematic perturbations is displayed in Figures 12c and 12d for the number of grid points. Also, in the three sets with 100% perturbations, the coefficient of variation for the number of grid points was about half of the value for the rate of hail precipitation (Figure 12c), whereas it has an equal magnitude to the value for total precipitation (Figure 12d). The starkly different uncertainty outcomes for hail precipitation and total precipitation, for both the intensity and the storm area, suggest that the uncertainty was strongly dependent on the

Figure 15. Same as Figure 10, but for the ensembles with perturbation magnitude reduced to 1.0×10^{-3} and 1.0×10^{-5} of the original perturbation, namely, EC_10^{-3}All and EC_10^{-5}All, respectively.

thermodynamic perturbations and uncertainty was larger in hail than in total precipitation under full perturbations. However, in the three sets with 10% perturbations, the coefficient of variation was not simply reduced to 10% of that of the sets with 100% perturbations, suggesting a nonlinear response of the uncertainty due to the perturbations of initial conditions. In the sets with 10% perturbations, there was a larger uncertainty in the rate than in the number of grid points for hail (Figures 12a and 12c), but the uncertainty in rate and number of grid points was similar for total precipitation (Figures 12b and 12d). Moreover, for the ensembles with 10% perturbations, the coefficient of variation for grid point coverage for total precipitation is larger than for hail precipitation, which is opposite to the behavior for the full perturbation ensembles (Figures 8c and 8d).

Although the importance of intrinsic predictability limits has been acknowledged in weather forecasting, its implications for the evaluation of cloud microphysics parameterizations has been less well addressed (Miltenberger et al., 2018). The uncertainty was also determined for the six hydrometeor species employed in the microphysics scheme, so that we could determine for which species the results were most uncertain under the different perturbations. The ensemble means of the six hydrometeor species were nondispersive under the six sets of perturbations during the evolution of the hailstorm (Figure 13). However, the ensemble spreads varied considerably, displaying a dispersive but regular time series under the different perturbations (Figure 14). The ensemble spread of EC_TQ was similar to that of EC_All for all hydrometeors, except hail, and was much larger than that of EC_UV, particularly in the three ice-phase species (ice, snow, and graupel). For the hail mass mixing ratio, EC_TQ generated the largest ensemble spread, followed by EC_All and EC_UV. Similarly, in the three sets of 10% perturbations, there was a comparative ensemble spread in EC_10%TQ and EC_10%All, both of which were larger than the ensemble spread of EC_10%UV. This suggests that the thermodynamic perturbations resulted in a larger uncertainty than did the kinematic perturbations for the six hydrometeor species in the simulated hailstorm, with the largest uncertainty in ice-phase species. This makes sense, given that thermodynamic perturbations strongly control the environmental instability, and thus overall storm strength, which is directly related to hydrometeor production.

The nonlinear reduction in EC_10%All suggested that the predictability of hail precipitation may be inherently limited, even if the environmental uncertainties were reduced to 10% of the currently realistic magnitude of initial perturbations (Figures 10b and 10d). The result of nonlinear reduction in hail precipitation is consistent with previous studies: For example, the intrinsic predictability limit has been found in a tornadic supercell case (Zhang et al., 2016), and substantial nonlinear reductions in the forecast spread for the structural features of a supercell were found in simulations with reduced magnitude of spread of their original initial conditions (Flora et al., 2018). To determine the robustness of our results for the intrinsic predictability of hail precipitation rate, we ran two additional ensemble groups with perturbations reduced to even smaller magnitudes: 1.0×10^{-3} and 1.0×10^{-5} of the original perturbations. The ensemble spread of hail precipitation in EC_1.0^{-3}All and EC_1.0^{-5}All still existed but reduced to smaller magnitudes than the initial condition perturbation magnitude reduction (Figure 15b), suggesting an even more obvious nonlinear response with smaller perturbations. Meanwhile, the similar performance could also be found in ensemble spread of total precipitation (Figure 15d). This is an indication of an existing intrinsic predictability limit for both hail precipitation rate and total precipitation rate before storm demise.

4. Conclusion

Using ensembles of convection-allowing (500-m horizontal grid spacing) WRF simulations of an idealized hailstorm, with realistic initial condition perturbations extracted from ECMWF operational ensemble analyses, we examined the sensitivity of hail precipitation rate to instantaneous environmental initial condition uncertainties, representing flow-dependent uncertainty. This study mainly focused on what type of initial condition perturbations (i.e., thermodynamic or kinematic) resulted in the greatest sensitivity in the hail rate and determined the magnitude of uncertainty in the hail rate.

The evolution of hail precipitation rate was highly sensitive to small perturbations in the initial conditions, particularly thermodynamic perturbations. We investigated how tiny differences in the realistic initial condition perturbations might influence hail rate using two selected groups of ensembles, with the top 10 maximum and bottom 10 minimum hail rates. Analyses in the EC_All set showed that perturbations in the initial conditions significantly affected the simulated hail precipitation rate. There was also very substantial variation in the parent storm itself and in its total precipitation rate: Significant differences were found in updraft speed and microphysical properties and processes. Together, these led to dramatic differences in the hail precipitation fields.

A comparison between the groups with separate thermodynamic and kinematic perturbations showed that the ensemble spread of the hail rate in groups with thermodynamic perturbations was significantly larger than in groups with kinematic perturbations, even when the magnitude of the initial perturbations was reduced to 10%. In part, this is due to the fact that perturbations were vertically correlated (i.e., they came from each of the 50 ECMWF ensemble members). Given the strong variability in CAPE near the storm (cf. Figure 1; the ensemble standard deviation is large enough to explain the differences in updraft speed between Top10 and Bottom10 members), even small perturbations in thermodynamics (when correlated vertically) could lead to substantial perturbations in CAPE, and thus much stronger storms. The kinematic perturbations, on the other hand, did not lead to as much ensemble spread in hail precipitation rate. This is likely because of the much reduced spatial variability of kinematic properties and that the magnitude of the perturbations was likely too small to significantly affect storms in a strongly sheared environment (e.g., compare to the much larger variations in vertical wind shear explored by Dennis & Kumjian, 2017).

In addition to this assessment of practical predictability, we investigated the intrinsic predictability of hail precipitation rate. To assess the intrinsic predictability of hail, a number of ensembles were constructed with initial condition perturbations reduced to 10%, 1.0×10^{-3}, and 1.0×10^{-5} of the currently realistic magnitude of initial condition perturbations available from ECMWF. A reduction in the magnitude of the initial perturbations in EC_10%All, EC_10^{-3}All, and EC_10^{-5}All produced substantial reductions in the ensemble spread of the hail rate and related cloud properties; however, the magnitude of the reduction was nonlinear, which suggests inherently limited predictability for hail precipitation and total precipitation rate. Finally, the uncertainties in hail precipitation rate were much larger than the uncertainties in total precipitation rate, with the coefficient of variation for the hail rate (>100%) being more than twice that of the coefficient of variation for the total precipitation rate. The uncertainties of the six hydrometeor species used in the

microphysics scheme were also assessed, with a larger uncertainty found for ice-phase particles than for liquid particles under thermodynamic perturbations.

Hail is a high-impact phenomenon, and therefore, the prediction of storm development and accurate microphysical parameterization is crucial for high-resolution simulations of hailstorms. Moreover, the differences in the hail precipitation and total precipitation fields are not tightly linked; for example, total precipitation rates from predicted storms do not make an exact proxy for hail precipitation rates as the strongest hail precipitation members are not simply the same as the strongest total precipitation members (Figure 5). Unfortunately, the uncertainty in different microphysics schemes is still not completely quantified. Due to a low vertical resolution in the ECMWF ensemble, low-level variations (e.g., low-level wind shear) among the ensemble members may not be captured representatively. Considerable uncertainty remains in our understanding and modeling of deep convective clouds and their nonlinear interactions with different processes, because model grid scales are typically several orders of magnitude larger than the process scales (Miltenberger et al., 2018). Real atmospheric conditions are much more complicated than the idealized conditions proposed here, particularly in environments favorable for deep convection. The uncertainty of hail precipitation rate might be case dependent, and therefore, more cases need to be investigated to reach general conclusions.

References

Allen, J. T., & Tippett, M. K. (2015). The characteristics of United States hail reports: 1955–2014. *Electronic Journal of Severe Storms Meteorology*, *10*(3), 1–31.

Cintineo, R. M., & Stensrud, D. J. (2013). On the predictability of supercell thunderstorm evolution. *Journal of the Atmospheric Sciences*, *70*(7), 1993–2011. https://doi.org/10.1175/JAS-D-12-0166.1

Dennis, E. J., & Kumjian, M. R. (2017). The impact of vertical wind shear on hail growth in simulated supercells. *Journal of the Atmospheric Sciences*, *74*(3), 641–663. https://doi.org/10.1175/JAS-D-16–0066.1

Duan, J., Chen, Y., & Guo, X. L. (2012). Characteristics of aerosol activation efficiency and aerosol and CCN vertical distributions in North China. *Acta Meteorologica Sinica*, *26*(5), 579–596. https://doi.org/10.1007/s13351–012–0504–6

Durran, D. R., & Weyn, J. A. (2016). Thunderstorms do not get butterflies. *Bulletin of the American Meteorological Society*, *97*(2), 237–243. https://doi.org/10.1175/BAMS-D-15–00070.1

Emanuel, K., & Zhang, F. (2017). The role of inner-core moisture in tropical cyclone predictability and practical forecast skill. *Journal of the Atmospheric Sciences*, *74*(7), 2315–2324. https://doi.org/10.1175/JAS-D-17–0008.1

Fernández-González, S., Martín, M. L., Merino, A., Sánchez, J. L., & Valer, F. (2017). Uncertainty quantification and predictability of wind speed over the Iberian Peninsula. *Journal of Geophysical Research: Atmospheres*, *122*, 3877–3890. https://doi.org/10.1002/2017JD026533

Flora, M. L., Potvin, C. K., & Wicker, L. J. (2018). Practical predictability of supercells: Exploring ensemble forecast sensitivity to initial condition spread. *Monthly Weather Review*, *146*(8), 2361–2379. https://doi.org/10.1175/MWR-D-17–0374.1

Guan, Y., Zheng, F., Zhang, P., & Qin, C. (2015). Spatial and temporal changes of meteorological disasters in China during 1950–2013. *Natural Hazards*, *75*(3), 2607–2623. https://doi.org/10.1007/s11069–014–1446–3

Kumjian, M. R., Ganson, S., & Ryzhkov, A. (2012). Raindrop freezing in deep convective updrafts: A microphysical and polarimetric model. *Journal of the Atmospheric Sciences*, *69*(12), 3471–3490. https://doi.org/10.1175/JAS-D-12-067.1

Li, M., Zhang, F., Zhang, Q., Harrington, J. Y., & Kumjian, M. R. (2017). Nonlinear response of hail precipitation rate to environmental moisture content: A real case modeling study of an episodic midlatitude severe convective event. *Journal of Geophysical Research: Atmospheres*, *122*, 6729–6747. https://doi.org/10.1002/2016JD026373

Li, X., Zhang, Q., & Xue, H. (2017). The role of initial cloud condensation nuclei concentration in hail using the WRF NSSL 2-moment microphysics scheme. *Advances in Atmospheric Sciences*, *34*(9), 1106–1120. https://doi.org/10.1007/s00376–017–6237–9

Lorenz, E. N. (1969). The predictability of a flow which possesses many scales of motion. *Tellus*, *21*(3), 289–307. https://doi.org/10.3402/tellusa.v21i3.10086

Mansell, E. R., & Ziegler, C. L. (2013). Aerosol effects on simulated storm electrification and precipitation in a two-moment bulk microphysics model. *Journal of the Atmospheric Sciences*, *70*(7), 2032–2050. https://doi.org/10.1175/JAS-D-12–0264.1

Mansell, E. R., Ziegler, C. L., & Bruning, E. C. (2010). Simulated electrification of a small thunderstorm with two-moment bulk microphysics. *Journal of the Atmospheric Sciences*, *67*(1), 171–194. https://doi.org/10.1175/2009JAS2965.1

Miglietta, M. M., Manzato, A., & Rotunno, R. (2016). Characteristics and predictability of a supercell during HyMeX SOP1. *Quarterly Journal of the Royal Meteorological Society*, *142*(700), 2839–2853. https://doi.org/10.1002/qj.2872

Miglietta, M. M., Mazon, J., & Rotunno, R. (2017). Numerical simulations of a tornadic supercell over the Mediterranean. *Weather and Forecasting*, *32*(3), 1209–1226. https://doi.org/10.1175/WAF-D-16–0223.1

Miltenberger, A. K., Field, P. R., Hill, A. A., Shipway, B. J., & Wilkinson, J. M. (2018). Aerosol–cloud interactions in mixed-phase convective clouds–Part 2: Meteorological ensemble. *Atmospheric Chemistry and Physics*, *18*(14), 10,593–10,613. https://doi.org/10.5194/acp-18–10593–2018

Molteni, F., Buizza, R., Palmer, T., & Petroliagis, T. (1996). The ECMWF ensemble prediction system: Methodology and validation. *Quarterly Journal of the Royal Meteorological Society*, *122*(529), 73–119. https://doi.org/10.1002/qj.49712252905

Morrison, H., & Milbrandt, J. (2011). Comparison of two-moment bulk microphysics schemes in idealized supercell thunderstorm simulations. *Monthly Weather Review*, *139*(4), 1103–1130. https://doi.org/10.1175/2010MWR3433.1

Morrison, H., Thompson, G., & Tatarskii, V. (2009). Impact of cloud microphysics on the development of trailing stratiform precipitation in a simulated squall line: Comparison of one- and two-moment schemes. *Monthly Weather Review*, *137*(3), 991–1007. https://doi.org/10.1175/2008MWR2556.1

Munsell, E. B., & Zhang, F. (2014). Prediction and uncertainty of Hurricane Sandy (2012) explored through a real-time cloud-permitting ensemble analysis and forecast system assimilating airborne Doppler radar observations. *Journal of the Atmospheric Sciences*, *6*(1), 38–58. https://doi.org/10.1002/2013ms000297

Munsell, E. B., Zhang, F., Sippel, J. A., Braun, S. A., & Weng, Y. (2017). Dynamics and predictability of the intensification of Hurricane Edouard (2014). *Journal of the Atmospheric Sciences*, *74*(2), 573–595. https://doi.org/10.1175/JAS-D-16–0018.1

Nielsen, E. R., & Schumacher, R. S. (2016). Using convection-allowing ensembles to understand the predictability of an extreme rainfall event. *Monthly Weather Review*, *144*(10), 3651–3676. https://doi.org/10.1175/MWR-D-16–0083.1

Potvin, C. K., Murillo, E. M., Flora, M., & Wheatley, D. M. (2017). Sensitivity of supercell simulations to initial-condition resolution. *Journal of the Atmospheric Sciences*, *74*(1), 5–26. https://doi.org/10.1175/JAS-D-16–0098.1

Punge, H. J., & Kunz, M. (2016). Hail observations and hailstorm characteristics in Europe: A review. *Atmospheric Research*, *176-177*, 159–184. https://doi.org/10.1016/j.atmosres.2016.02.012

Snook, N., Jung, Y., Brotzge, J., Putnam, B., & Xue, M. (2016). Prediction and ensemble forecast verification of hail in the supercell storms of 20 May 2013. *Weather and Forecasting*, *31*(3), 811–825. https://doi.org/10.1175/WAF-D-15–0152.1

Weyn, J. A., & Durran, D. R. (2017). The dependence of the predictability of mesoscale convective systems on the horizontal scale and amplitude of initial errors in idealized simulations. *Journal of the Atmospheric Sciences*, *74*(7), 2191–2210. https://doi.org/10.1175/JAS-D-17–0006.1

Weyn, J. A., & Durran, D. R. (2018). Ensemble spread grows more rapidly in higher-resolution simulations of deep convection. *Journal of the Atmospheric Sciences*, *75*(10), 3331–3345. https://doi.org/10.1175/JAS-D-17–0332.1

Zhang, F., Odins, A. M., & Nielsen-Gammon, J. W. (2006). Mesoscale predictability of an extreme warm-season precipitation event. *Weather and Forecasting*, *21*(2), 149–166. https://doi.org/10.1175/WAF909.1

Zhang, F., & Sippel, J. A. (2009). Effects of moist convection on hurricane predictability. *Journal of the Atmospheric Sciences*, *66*(7), 1944–1961. https://doi.org/10.1175/2009JAS2824.1

Zhang, F., & Tao, D. (2013). Effects of vertical wind shear on the predictability of tropical cyclones. *Journal of the Atmospheric Sciences*, *70*(3), 975–983. https://doi.org/10.1175/JAS-D-12–0133.1

Zhang, Y., Zhang, F., Stensrud, D. J., & Meng, Z. (2015). Practical predictability of the 20 May 2013 tornadic thunderstorm event in Oklahoma: Sensitivity to synoptic timing and topographical influence. *Monthly Weather Review*, *143*(8), 2973–2997. https://doi.org/10.1175/MWR-D-14–00394.1

Zhang, Y., Zhang, F., Stensrud, D. J., & Meng, Z. (2016). Intrinsic predictability of the 20 May 2013 tornadic thunderstorm event in Oklahoma at storm scales. *Monthly Weather Review*, *144*(4), 1273–1298. https://doi.org/10.1175/MWR-D-15–0105.1